Needle optical coherence elastography for the measurement of microscale mechanical contrast deep within human breast tissues

Kelsey M. Kennedy
Robert A. McLaughlin
Brendan F. Kennedy
Alan Tien
Bruce Latham
Christobel M. Saunders
David D. Sampson

SPIE

Needle optical coherence elastography for the measurement of microscale mechanical contrast deep within human breast tissues

Kelsey M. Kennedy,[a] Robert A. McLaughlin,[a] Brendan F. Kennedy,[a] Alan Tien,[b] Bruce Latham,[c] Christobel M. Saunders,[b] and David D. Sampson[a,d]
[a]University of Western Australia, School of Electrical, Electronic & Computer Engineering, Optical+Biomedical Engineering Laboratory, 35 Stirling Highway, Crawley, Western Australia 6009, Australia
[b]University of Western Australia, School of Surgery, 35 Stirling Highway, Crawley, Western Australia 6009, Australia
[c]PathWest, 197 Wellington Street, Perth, Western Australia 6000, Australia
[d]University of Western Australia, Centre for Microscopy, Characterisation & Analysis, 35 Stirling Highway, Crawley, Western Australia 6009, Australia

Abstract. Optical coherence elastography (OCE) is an emerging imaging technique that probes microscale mechanical contrast in tissues with the potential to differentiate healthy and malignant tissues. However, conventional OCE techniques are limited to imaging the first 1 to 2 mm of tissue in depth. We demonstrate, for the first time, OCE measurements deep within human tissues using needle OCE, extending the potential of OCE as a surgical guidance tool. We use needle OCE to detect tissue interfaces based on mechanical contrast in both normal and malignant breast tissues in freshly excised human mastectomy samples, as validated against histopathology. Further, we demonstrate the feasibility of *in situ* measurements >4 cm from the tissue surface using ultrasound guidance of the OCE needle probe. With further refinement, our method may potentially aid in accurate detection of the boundary of the tumor to help ensure full removal of all malignant tissues, which is critical to the success of breast-conserving surgery. © *2013 Society of Photo-Optical Instrumentation Engineers (SPIE)* [DOI: 10.1117/1.JBO.18.12.121510]

Keywords: optical coherence tomography; elastography; needle probe; breast cancer; mechanical properties.

Paper 130457SSRR received Jul. 2, 2013; revised manuscript received Nov. 15, 2013; accepted for publication Nov. 20, 2013; published online Dec. 23, 2013.

1 Introduction

Breast cancer is the most commonly diagnosed cancer in females worldwide and the second leading cause of cancer-related deaths in females in North America, Europe, and Australia.[1] A common surgical treatment is breast-conserving surgery, or lumpectomy, in which the tumor and a margin of healthy surrounding tissue are excised, while the remainder of the breast is preserved. The efficacy of breast-conserving surgery in the treatment of breast cancer relies on obtaining clear tumor margins, i.e., the boundary of the excised tissue must be free of malignancy. Tumor margins are currently assessed by postoperative histological examination. Positive and close tumor margins (tumor cells found at the boundary of the excised tissue and within 1 to 5 mm of the boundary, respectively) are correlated with an increased risk of local recurrence of the disease, and often necessitate additional surgery or aggressive postoperative radiation treatments.[2] Currently, approximately 23% of women who undergo breast-conserving surgery must return for additional surgery due to insufficient margins.[3] Improved guidance of tumor excision and intraoperative assessment of tumor margins have the potential to reduce the need for re-excision.

Currently, surgeons manually palpate, or feel, the tissue to find the boundaries of the tumor and to guide excision, as many breast tumors manifest as stiff lesions. However, some cancers present as nonpalpable lesions, i.e., they are too small or soft to detect through touch or may have a permeative growth pattern that results in a poorly delineated mass with small extensions of malignancy.[4] In these nonpalpable cases, hookwire guidance is commonly used, in which a wire is placed in the tumor mass under radiological guidance prior to surgery. The surgeon then excises an area of tissue around the wire according to the tumor size estimated by preoperative imaging. However, tissue can deform between preoperative imaging and surgery, and extensions of malignancy beyond the bulk tumor mass are not always detectable using conventional medical imaging modalities such as ultrasound, x-ray, and magnetic resonance imaging, making this technique imprecise.[5] Furthermore, if the size of the lesion is overestimated, then an unnecessarily large amount of tissue may be removed, degrading the preservation of cosmesis. Once the lesion is excised, intraoperative assessment of tumor margins is sometimes performed using frozen-section analysis, but this process is time-consuming, taking ~25 min on average[6] and, importantly, has had only limited success in reducing overall re-excision rates.[7] Thus, there remains a need for an intraoperative guidance technique that can detect the precise boundaries of the tumor to ensure that sufficient tumor margins are obtained and ultimately reduce the number of re-excisions performed.

Optical coherence tomography (OCT) provides three-dimensional (3-D) images of tissue microstructure with a high resolution of ~10 μm and a penetration depth in scattering tissue

Address all correspondence to: Kelsey M. Kennedy, University of Western Australia, School of Electrical, Electronic and Computer Engineering (M018), Optical+Biomedical Engineering Laboratory, 35 Stirling Highway, Crawley, Western Australia 6009, Australia. Tel: +61 8 6488 2317; Fax: +61 8 6488-1319; E-mail: 20413465@student.uwa.edu.au

of 1 to 2 mm and can be performed *in vivo*, making it a suitable candidate for intraoperative detection of tumor boundaries.[8–10] However, the contrast in the OCT images, produced largely by optical scattering, is sometimes insufficient for tissue differentiation. For example, collagenous connective tissues of the breast can appear similar to dense tumor.[8–10] Additional contrast mechanisms would assist OCT to more readily distinguish tumor from normal breast tissues.

The changes in tissue's constituent materials and microstructure that occur with the onset of breast cancer lead to changes in the local mechanical properties of the tissue. The spread of cancer cells in the breast is often accompanied by desmoplasia, the rapid production of collagen as stroma to structurally support the rapidly growing tumor. It is the presence of this dense stroma that causes many tumors to feel stiff to the touch.[11] On a cellular level, individual tumor cells actually tend to be softer than normal epithelial cells in the breast.[12] Reports have suggested that this facilitates their migration and metastasis.[13] These mechanical characteristics in malignant tumors make them distinct from healthy tissues. Thus, probing the mechanical properties of tissue during breast-conserving surgery could potentially provide additional contrast between healthy and malignant tissues and aid identification of tumor boundaries.

Optical coherence elastography (OCE) is an extension to OCT that probes the mechanical properties of tissue on the microscale.[14,15] OCE is performed by applying a load to tissue and measuring the resulting local displacements within the tissue using OCT. From the displacements, a distribution of mechanical properties may be estimated. OCE is an optical analogue of elastography techniques previously developed using ultrasound and magnetic resonance imaging. These techniques map mechanical properties with coarser spatial resolution than OCE, but over a wider field-of-view, and have been shown to provide additional contrast to complement the underlying imaging technique and to aid in the diagnosis of breast lesions.[16–18] OCE has been demonstrated *in vivo*,[19–21] proposed for soft tissue tumor detection,[22] and shown potential for providing contrast between malignant and normal tissues of the breast.[23,24] However, OCE has so far been restricted to imaging the first 1 to 2 mm of tissue in depth, which limits its utility for the detection of tumor boundaries situated farther below the tissue surface. Preliminary results measuring the velocity of surface acoustic waves[25,26] have shown potential to probe depth-dependent mechanical properties beyond the penetration depth of OCT; sensitivity to changes in stiffness up to 55 mm below the surface has been reported using holographic detection.[25] However, these techniques come at a loss of lateral resolution (0.5 to 1 mm), primarily due to the wavelength of the generated surface wave, typically >10 mm.

The recent development of OCT needle probes[27–32] has enabled imaging of tissue microstructure, including breast tumor margins[27,29] centimeters below the tissue surface. We recently developed a technique to perform one-dimensional (1-D) OCE measurements via an OCT needle probe.[33] Our technique, needle OCE, detects mechanical contrast by measuring the depth-resolved mechanical response of tissue to needle insertion. Our initial results demonstrated the detection of boundaries in tissue-mimicking phantoms and in *ex vivo* porcine airway wall.[33]

Here, with a view toward improving guidance of breast-conserving surgery, we report the use of needle OCE to detect tissue boundaries in human breast tissues. We demonstrate the ability

of needle OCE to distinguish tissue types in freshly excised (not fixed) human breast tissue samples comprising adipose, connective tissues and tumor. These needle OCE measurements are the first obtained deep within tissue, as previous measurements were obtained by, in effect, indenting the tissue surface.[33] We also demonstrate the feasibility of needle OCE to detect tumor boundaries *in situ*, using ultrasound guidance of the needle probe[27] to detect a tumor boundary at a depth of several centimeters below the tissue surface in a human mastectomy sample. The results demonstrate the first mechanical contrast in tissue detected at such depths using OCE and point to the potential of needle OCE as an intraoperative guidance tool.

2 Methods

2.1 System Setup and Needle OCE Method

Figure 1 illustrates the OCE system and forward-facing needle probe design employed in this study. The distal end of the optical fiber probe, designed to operate in the 800-nm wavelength range, consists of a single-mode fiber fusion spliced to a 270-μm length of gradient-index (GRIN) fiber. A common-path interferometric configuration was used with the GRIN end face serving as the reference backreflection. The length of the GRIN fiber was selected such that a collimated beam would result at the fiber exit, maximizing the reference backreflection power and, thus, the probe's sensitivity. This fiber length was determined from simulations using the paraxial ray-matrix formalism for Gaussian beams.[34] The measured $1/e^2$ beam diameter was 19 μm at a distance of 20 μm from the bare probe end face, and the measured depth of focus in air was 310 μm. The optics are fixed inside a hypodermic needle using an optical adhesive (Norland, Cranbury, New Jersey). Two needle gauges (G) were used in this study: 20G (0.9-mm outer diameter) and 22G (0.7-mm outer diameter).

To perform the measurements, the needle probe was coupled to a custom-built, portable, spectral-domain OCT (SD-OCT) system. The light source is a superluminescent diode with a central wavelength of 835 nm and a bandwidth of 50 nm. The measured axial resolution is 8.5 μm in air. A motorized translation stage was used to advance the needle at 50 μm/s for all measurements, and A-scans were acquired at a rate of
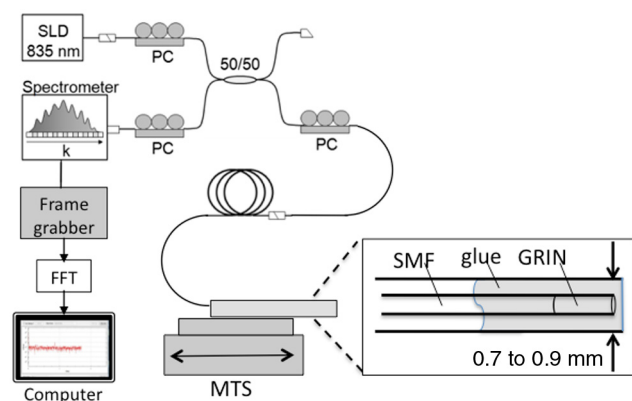

Fig. 1 Schematic of spectral-domain optical coherence tomography (SD-OCT) system and forward-facing needle probe (SLD: superluminescent diode; PC: polarization controller; FFT: fast Fourier transform; MTS: motorized translation stage; SMF: single-mode fiber; GRIN: gradient-index fiber).

5 kHz during insertion. To measure the tissue deformation ahead of the needle during insertion, we employed a phase-sensitive method, calculating the depth-resolved tissue displacements from the phase difference between sequential A-scans,[35] as illustrated in Fig. 2. The phase sensitivity of the system was measured to be 7.7 mrad at an OCT signal-to-noise ratio (SNR) of 50 dB, corresponding to a displacement sensitivity of 340 pm.

The magnitude and direction of tissue displacement ahead of the needle depend on the needle tip geometry as well as on the tissue mechanical properties. As the phase-sensitive method detects only the axial component of tissue motion (i.e., along the incident light beam), it is important to maximize this axial motion for optimal sensitivity to mechanical contrast. We therefore employed a flat needle tip, which maximizes compression of the tissue ahead of the needle,[36] resulting in a large axial component of displacement. Note that a sharp needle tip was not used, as this would maximize the degree of tissue cutting directly ahead of the tip, potentially resulting in gaps between the needle probe and the tissue and complicating measurement and interpretation of axial tissue displacements.

Upon needle insertion, compression of the tissue ahead of the needle results in maximum tissue displacement at the needle tip and a decrease in displacement with distance from the needle. We note that although compression can alter the group refractive index of tissue, potentially offsetting the measured displacement values, this effect will be negligible for the small strains induced by the nanometer-scale movement of the needle between A-scans. Strain may be estimated in these measurements as the derivative of displacement versus depth.[37] It is inversely related to the Young's modulus, or stiffness, under the assumption of uniform stress in the region of tissue probed. In Ref. 33, we demonstrated in phantoms containing inclusions of known Young's modulus that a change in strain determined by a needle
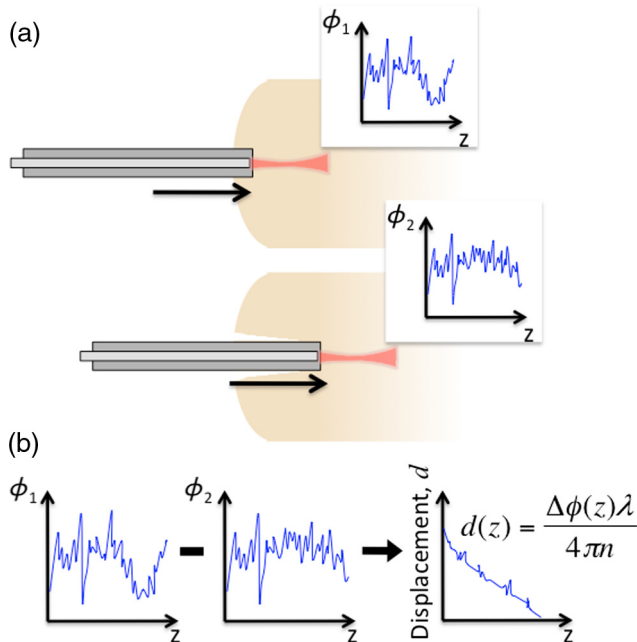
OCE measurement indicates a mechanical interface. It was also demonstrated that the relative strains depend not only on the relative Young's moduli of the tissues, but also on the proximity of the needle to a mechanical interface. For example, as the needle approaches a stiff lesion, the soft tissue between the needle tip and the lesion will become more compressed, resulting in higher strain. Thus, such strain measurements can localize tissue interfaces, but can only give a qualitative estimate of the relative Young's modulus of tissues without the knowledge of the local stresses in the sample.[38,39]

2.2 Experiments in Human Breast Tissue

Excised human mastectomy samples from patients undergoing breast cancer surgery were scanned immediately following excision ($n = 5$), and all scans were completed within 4 h of excision. The Human Research Ethics Committee of Royal Perth Hospital approved the study, and informed consent was obtained from the patients. Two types of scanning were performed, as illustrated in Fig. 3. In the first experimental setup, to assess the ability of needle OCE to detect contrast between various breast tissues, small samples ($\sim$1 cm^3 in volume) comprising distinct regions of tissue were cut from four of the breast mastectomy specimens. This allowed the needle probe to be inserted into the samples with a known trajectory, facilitating later histological validation. However, we observed that the insertion of the needle probe into such small samples does
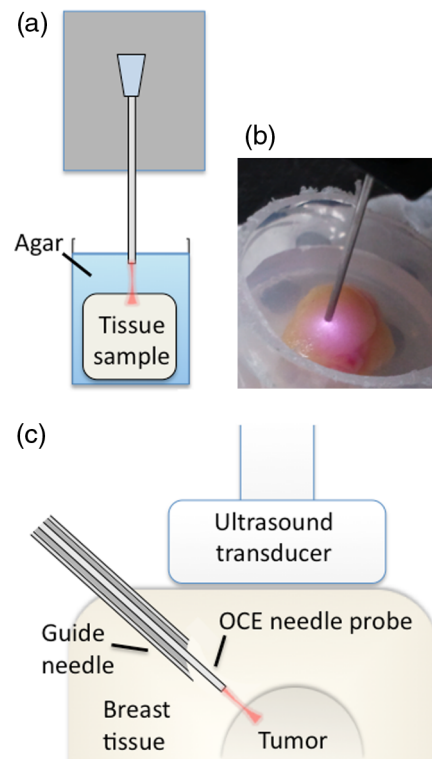

Fig. 2 Method for the measurement of tissue displacement in needle optical coherence elastography (OCE). (a) Measurements of the phase of the OCT A-scans are acquired at two incremental needle probe positions. (b) The phase difference between the two A-scans, $\Delta\phi = \phi_1 - \phi_2$, is linearly related to axial tissue displacement.

Fig. 3 Schematics of experimental setups for needle OCE measurements in human breast tissues. (a) Setup for small excised breast tissue samples and (b) photograph of an experiment. Samples were embedded in agar solution to simulate needle insertion into a large mass of tissue. (c) Setup for *in situ* ultrasound-guided measurements in a full mastectomy sample. Guide needle was used to aid positioning of the needle OCE probe and to facilitate histological sectioning following measurements.

not elicit a response representative of the tissue *in situ* because of the significant impact of boundary conditions in small samples. Therefore, these small samples were embedded in agar solution to simulate the tissue being held within a larger sample, as seen in Fig. 3(a). This also served to reduce bulk motion of the sample, such that only tissue displacement due to insertion was measured. The agar solution was heated to liquid form and then placed on ice to rapidly cool to room temperature, forming a soft solid. During cooling, the tissue was embedded in the agar solution and held using forceps in an orientation suitable for scanning while the surrounding agar solidified. Samples were kept hydrated in a saline solution prior to embedding in agar and scanning. Following measurements, the tissue samples were bisected along the axis of needle probe insertion, and hematoxylin and eosin (H&E)-stained sections were prepared in the plane of the bisection using standard pathology techniques.

In the second experimental setup, to demonstrate the feasibility of needle OCE for *in situ* measurements, measurements were performed on one full mastectomy sample, in which the tumor was situated several centimeters below the tissue surface. Ultrasound guidance was used to direct the needle toward the tumor mass, following the protocol described in Ref. 27. Placement of the needle probe in proximity to the tumor was achieved by first inserting a sharp, 18G hollow guide needle toward the tumor under ultrasound guidance, as illustrated in Fig. 3(c). Unlike the needle probe, which used a flat tip to compress tissue, the guide needle employed a sharp tip to facilitate initial puncture and penetration into tissue. The 22G needle probe was then inserted through the guide needle to acquire measurements while advancing toward the tumor. An additional purpose of the guide needle was to indicate the exact location scanned for subsequent histological validation. For this reason, it was left *in situ* following needle OCE measurements. A slice was taken along the length of the guide needle, and H&E-stained sections were prepared from this face following the procedure used in Ref. 27.

3 Results

3.1 Needle OCE of Excised Human Breast Tissues

Figure 4 shows the results of needle OCE measurements in two breast samples [scanned using the setup in Fig. 3(a)] comprising adipose and normal stroma [Figs. 4(a)–4(d)] and adipose and tumor [Figs. 4(e)–4(h)], respectively. The H&E histology sections taken along the needle insertion path in these two samples verify the presence of the two tissue types. In each case, the 20G needle probe was inserted into the adipose and advanced toward the stroma or tumor, respectively. Motion-mode (M-mode) images of the structural OCT A-scans acquired versus time during needle insertion are shown in Figs. 4(b) and 4(f), in which the adipose tissue is distinguishable as a region of modulated signal due to higher reflectance at the cytoplasmic membrane of individual fat cells. The regions of stroma and tumor present as more homogeneously backscattering regions in these M-mode images. The M-mode images show the tissue interface drawing closer as the needle advances in the tissue. These trends in the backscattering signatures of the tissues are also apparent in the OCT A-scans Figs. 4(c) and 4(g), which are the average of 500 A-scans at the time points indicated by the dashed lines in the M-mode images. Note that the needle displacement during the acquisition of 500 A-scans is only 5 μm, which is less than
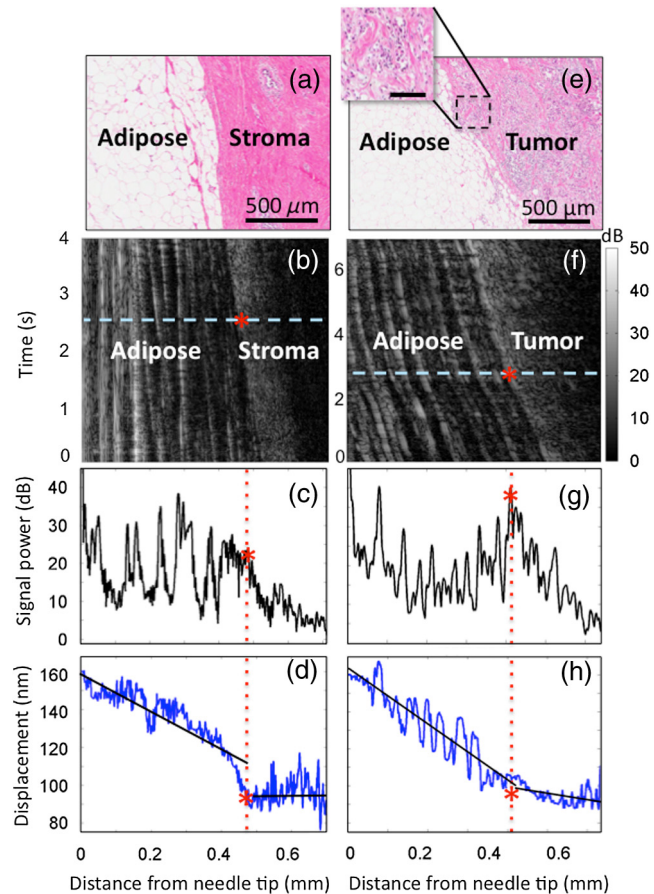

Fig. 4 Needle OCE of excised breast tissue samples comprising (a–d) adipose and dense stroma and (e–h) adipose and tumor. (a, e) Representative hematoxylin and eosin (H&E) histology section along the path of needle insertion, with inset in (e) showing tissue constituent detail (scale bar on inset 100 μm); (b, f) M-mode structural OCT image during needle insertion; (c, g) Average OCT A-scans at time point indicated by dashed lines in M-mode images; and (d, h) corresponding displacement ahead of the needle tip at these time points. The red stars indicate locations of the tissue interfaces estimated from the displacement data, and the slopes of the least-squares fitted black lines indicate local strain.

the axial resolution of the OCT system. Thus, these averaged A-scans provide, in effect, instantaneous 1-D structural information at the indicated time points.

The corresponding displacement traces at these time points are shown in Figs. 4(d) and 4(h). The black lines indicate least-squares fits to the displacement data in the two predominant tissue regions seen in the histology (in these cases, adipose/stroma and adipose/tumor). The fluctuations in the measured displacement in the adipose may be attributed to the corresponding fluctuations in OCT SNR as the phase variance, and, therefore, the variance of the measured displacements increase with lower OCT SNR. However, averaging of the 500 A-scans served to narrow this variance and to increase the displacement measurement accuracy. Thus, the fluctuations in displacement may also be a genuine effect of the differing mechanical responses of the outer membranes and lipid interiors of the individual cells. In either case, displacements measured at points with high SNR (corresponding to the adipose cell membranes) provide sufficient data to indicate the overall trend of displacement within the regions of adipose. Locations of sharp changes in the
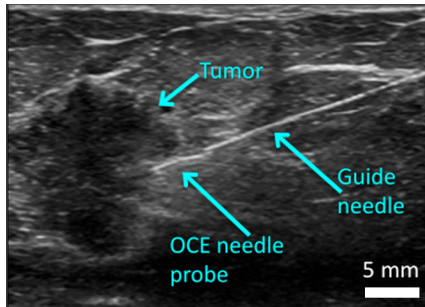
Fig. 5 Sonogram captured during ultrasound-guided needle OCE in a human mastectomy sample.

slope of the displacement, visually estimated from the displacement data, are denoted by red stars, which have also been placed at the same depth locations in the OCT M-mode images and A-scans (connected by the dotted red lines), to show the close correspondence of locations of the tissue interfaces detected using each type of data. In Fig. 4(d), a rapid decrease in displacement of the adipose with distance from the needle indicates high strain in this soft tissue. This strain was calculated as the slope of the fitted line to be 110 microstrain ($\mu\varepsilon$). By contrast, the dense stroma exhibits an approximately constant displacement with depth or ~0 strain, indicating that it is pushed away from the needle as a bulk. This is expected for tissue made up of such densely packed collagen.[40] The tissue composition is confirmed by the histology in Fig. 4(a).

In the case of needle insertion toward the tumor, Fig. 4(h), compression of the adipose is again apparent; the strain in this region, as calculated from the slope of the black line, is 150 $\mu\varepsilon$. The tumor also exhibits a small amount of strain (~30 $\mu\varepsilon$) rather than a bulk motion, as exhibited by the dense stroma in Fig. 4(d). This data suggest that portions of tissue consisting of intermingled, heterogeneous regions of tumor and collagen, as seen in the enlarged inset of histology for this sample in Fig. 4(e), may be more deformable than tissue that is homogenously

and densely packed with mature collagen fibers. As the local response of tissue to the needle is dependent on both the tissue constituents and the structural integrity with which the constituents are arranged, we hypothesize that this deformability may be a consequence of the compromised structural integrity of tissue infiltrated with areas of invasive malignant growth and also the relative softness of individual cancer cells.[12]

3.2 Tumor Boundary Detection Using Ultrasound-Guided Needle OCE in a Mastectomy Sample

Figure 5 shows an ultrasound image (sonogram) captured immediately prior to needle OCE measurements taken from within a full mastectomy sample. The needle probe can be seen protruding from the guide needle toward the tumor mass, which presents as a hypoechoic region in the image. The image demonstrates that the measurements were acquired when the needle was >4 cm beyond the tissue surface.

The results of these ultrasound-guided measurements are shown in Fig. 6. An M-mode image of the OCT A-scans acquired during insertion, Fig. 6(a), shows the characteristic modulated OCT signal generated from adipose cells as well as a region of more homogeneously backscattering tissue corresponding to tumor. A histology section prepared along the path of needle insertion, Fig. 6(b), also shows these two tissue types.

Figures 6(c) and 6(d) show the average of two sets of 500 OCT A-scans acquired at times 1 and 18 s, respectively, during needle insertion, as denoted by the cyan and green dashed lines in the M-mode image. The estimated locations in the tissue in which these scans were acquired are denoted by the cyan and green brackets on the histology image. Note that between these two time points, the needle advanced a total of 850 μm (17 s at 50 μm/s). However, as seen in the M-mode image, the tumor interface moves only ~100 μm closer to the needle tip, indicating that the needle was pushing the tumor away instead of continuously cutting through the tissue. The scan locations
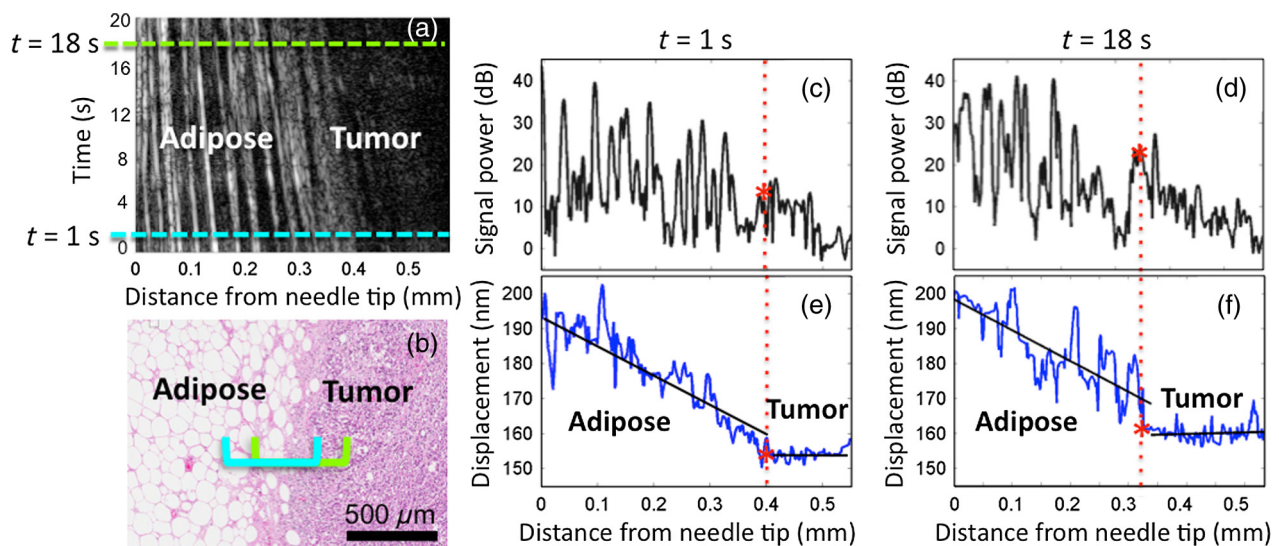

Fig. 6 Ultrasound-guided needle OCE results in a human mastectomy sample. (a) M-mode OCT image during needle insertion toward tumor. (b) Histology acquired along path of needle insertion. Cyan and green brackets mark the estimated regions of tissue scanned at $t = 1$ s and $t = 18$ s, respectively. (c, d) Average OCT A-scans and (e, f) corresponding displacement for time points indicated by the dashed cyan and green lines in (a). The red stars indicate locations of the tissue interfaces estimated from the displacement data, and the slopes of the least-squares fitted black lines indicate local strain.

indicated in the histology image were estimated based on this observation.

In the displacement traces, Figs. 6(e) and 6(f), the adipose tissue exhibits higher strain than the tumor, which moves as a bulk with ∼0 strain, indicating that this tumor interface is more rigid than that measured in Fig. 4(h). Also, as the needle advances, the adipose becomes more compressed between the needle and the tumor, which manifests as a slight increase in strain between the two time points [from 60 $\mu\varepsilon$ in Fig. 6(e) to 80 $\mu\varepsilon$ in Fig. 6(f)]. At each time point, the tissue interface can be easily detected based on a sharp change in strain, demonstrating the ability of the technique to detect the instantaneous location of the tumor boundary relative to the needle tip throughout the insertion. Also, although the region of adipose is easily identified in the OCT data, it is challenging to identify the boundary of the tumor based on the changes in the structural OCT signal. Importantly, the displacement data offers better contrast between the two tissue regions and more convincing identification of the tumor boundary.

4 Discussion

The results presented here demonstrate the ability of needle OCE to detect mechanical contrast between tissue types deep in human breast cancer samples. Using phase-sensitive OCT to measure the deformation of tissue due to needle insertion, tissue boundaries can be detected at depths several centimeters below the surface of the tissue.

The mechanical contrast detected by needle OCE is complementary to the scattering contrast detected using OCT and may in some cases be superior, as the scattering contrast alone can be inadequate for distinguishing regions of normal and malignant tissues.[8–10,29] This potential for improved contrast is demonstrated in the results in Fig. 6, where the boundary between adipose and tumor tissue in the mastectomy sample is notably more distinct in the displacement traces than in the individual OCT A-scans. We anticipate that the combined interpretation of the mechanical and scattering contrasts will enable more sensitive tumor boundary detection than either type of contrast on its own. Parametric analysis of OCT data could be incorporated to further enhance tissue contrast.[41] The addition of molecular contrast, e.g., that provided by fluorescence imaging, could also strengthen sensitivity to malignancy, and this may be possible with the recent development of a dual-modality needle probe that performs OCT and fluorescence imaging.[42]

Further studies are needed to assess the impact of needle insertion speed, tissue geometry, and stiffness contrast between features on the sensitivity of needle OCE to tissue interfaces. This can be achieved by performing measurements in a range of phantoms with controllable structural and mechanical properties.[43] Comparison of the measurements to finite element simulations of tissue deformation due to needle insertion would also improve understanding of the contrast detectable using needle OCE.[38,39] Such modeling studies, as well as continued measurements in larger numbers of breast tissue samples, will be essential for eventually establishing quantified criteria for automated detection of tumor boundaries using this technique. Furthermore, the measurements here provide qualitative information about the relative stiffness of the tissues, which in many cases may be sufficient for detecting the presence of malignant tissue. However, a measurement of stress imparted to the tissue may allow a quantitative assessment of tissue stiffness, and may enable longitudinal studies. Such a stress measurement could feasibly be achieved by incorporating a load cell on the proximal end of the needle.

In three of the four displacement measurements presented here, namely, in cases of needle insertion toward dense stroma in Fig. 4(d) and toward the tumor in the mastectomy samples in Figs. 6(e) and 6(f), we observed bulk motion (very low strain) of the nonadipose tissues. We hypothesize that this is partially due to the high stiffness of these tissues, as they were detectable by manual palpation, and may also be a result of the tissues' resistance to puncture by the needle probe. Although we have assumed here that the measured displacement is due to compression of the tissue ahead of the flat needle tip, insertion of the needle is also known to induce crack propagation.[36] Therefore, the displacement measurements are likely a function of both the tissue's stiffness and resistance to puncture (fracture toughness), and the measurement of axial strain may not always be sufficient for differentiating tissue types. This is another example where comparison of measurements to mechanical models of needle insertion is expected to aid in the understanding of tissue contrast.

The 1-D depth-resolved measurements provided by the current method can be used to detect mechanical contrast and to localize tissue boundaries. However, for the technique to eventually be used as a guidance tool, greater spatial sampling of the tissue would provide clearer delineation of tissue boundaries. Imaging the spatial variance of mechanical properties may also improve the technique's differentiation of malignant tissue from healthy stroma. Both tissue types exhibited bulk motion in the local measurements in this article but are known to present different degrees of spatial heterogeneity.[12] A number of scanning schemes have been proposed for optical needle probes that enable formation of 3-D structural images, including forward-facing designs,[44,45] in which the beam is scanned laterally from the front of the needle tip, as well as side-facing designs,[31,46,47] in which the beam exits from the side of the needle and the needle is rotated to acquire a two-dimensional (2-D) image. Implementation of elastography measurements into such an imaging probe design is expected to facilitate the translation of needle OCE toward clinically useful measurements. In particular, a forward-facing design, such as those proposed in Refs. 44 or 45, would preserve the ability to measure tissue deformation due to needle insertion ahead of the needle tip. The alternative 2-D implementation of OCE in a side-facing design will present additional challenges in developing strategies for synchronous tissue loading and detection of displacement. A potential solution may be to deliver focused ultrasound via the needle, applying an acoustic radiation force to the tissue.[48,49]

A handheld implementation of the probe may be necessary for clinical use, although the needle's actuating motion may still be automated for OCE acquisition. Such a handheld scenario may require faster acquisition speeds to reduce sensitivity to low-frequency motion artifacts, such as those potentially caused by involuntary motion of the surgeon or patient. External tracking of the needle probe position could be used to identify involuntary motions and to allow the acquired data to be corrected accordingly.[50] Furthermore, practical clinical use of needle OCE will require real-time interpretation of data, which may be facilitated by the conversion of the acquired signal to an audio output.[51]

Finally, breast-conserving surgery represents only one type of cancer surgery in which precise guidance of tumor resection

and assessment of margins are critical for predicting patient outcomes. In resection of cancerous tumors of the brain[52] and prostate,[53] for example, guidance of surgery is imperative not only to ensure complete tumor removal, but also to prevent damage to healthy tissues to preserve vital functions and quality of life. We anticipate that in addition to breast-conserving surgery, needle OCE may have applications in surgical guidance for other soft tissue tumors, in which probing mechanical properties may also provide additional contrast between normal and malignant tissues.

5 Conclusion

Needle OCE has significant potential for the *in situ* assessment of tumor margins. This article presents the first needle OCE measurements of human breast tissues, showing an ability to detect the boundary between normal adipose and malignant tissue with results validated against co-located histology. We have demonstrated the potential of this technique to detect a tumor interface deep within a mastectomy sample with measurements acquired >4 cm below the tissue surface. These preliminary results demonstrate the feasibility of this technique to measure contrast based on the mechanical properties of tissue, complementing the optical contrast in the corresponding OCT A-scan data, with the potential to improve guidance of breast-conserving surgery.

References

1. American Cancer Society, *Global Cancer Facts & Figures*, 2nd ed., American Cancer Society, Atlanta (2011).
2. M. F. Dillon et al., "A pathologic assessment of adequate margin status in breast-conserving therapy," *Ann. Surg. Oncol.* **13**(3), 333–339 (2006).
3. L. E. McCahill et al., "Variability in reexcision following breast conservation surgery," *J. Am. Med. Assoc.* **307**(5), 467–475 (2012).
4. C. W. Sewell, "Pathology of benign and malignant breast disorders," *Radiol. Clin. N. Am.* **33**(6), 1067–1080 (1995).
5. R. G. Pleijhuis et al., "Obtaining adequate surgical margins in breast-conserving therapy for patients with early-stage breast cancer: current modalities and future directions," *Ann. Surg. Oncol.* **16**(10), 2717–2730 (2009).
6. O. Riedl et al., "Intraoperative frozen section analysis for breast-conserving therapy in 1016 patients with breast cancer," *Eur. J. Surg. Oncol.* **35**(3), 264–270 (2009).
7. N. Cabioglu et al., "Role for intraoperative margin assessment in patients undergoing breast-conserving surgery," *Ann. Surg. Oncol.* **14**(4), 1458–1471 (2007).
8. P. L. Hsiung et al., "Benign and malignant lesions in the human breast depicted with ultrahigh resolution and three-dimensional optical coherence tomography," *Radiology* **244**(3), 865–874 (2007).
9. F. T. Nguyen et al., "Intraoperative evaluation of breast tumor margins with optical coherence tomography," *Cancer Res.* **69**(22), 8790–8796 (2009).
10. R. Patel et al., "Delineating breast ductal carcinoma using combined dye-enhanced wide-field polarization imaging and optical coherence tomography," *J. Biophotonics* **6**(9), 679–686 (2013).
11. R. A. Walker, "The complexities of breast cancer desmoplasia," *Breast Cancer Res.* **3**(3), 143–145 (2001).
12. M. Plodinec et al., "The nanomechanical signature of breast cancer," *Nat. Nanotechnol.* **7**(11), 757–765 (2012).
13. S. Suresh, "Biomechanics and biophysics of cancer cells," *Acta Mater.* **55**(12), 3989–4014 (2007).
14. J. Schmitt, "OCT elastography: imaging microscopic deformation and strain of tissue," *Opt. Express* **3**(6), 199–211 (1998).
15. C. Sun, B. Standish, and V. X. D. Yang, "Optical coherence elastography: current status and future applications," *J. Biomed. Opt.* **16**(4) 043001 (2011).
16. S. Wojcinski et al., "Multicenter study of ultrasound real-time tissue elastography in 779 cases for the assessment of breast lesions: improved diagnostic performance by combining the BI-RADS®-US classification system with sonoelastography," *Ultraschall Med.* **31**(5), 484–491 (2010).
17. M. Tanter et al., "Quantitative assessment of breast lesion viscoelasticity: initial clinical results using supersonic shear imaging," *Ultrasound Med. Biol.* **34**(9), 1373–1386 (2008).
18. Y. K. Mariappan, K. J. Glaser, and R. L. Ehman, "Magnetic resonance elastography: a review," *Clin. Anat.* **23**(5), 497–511 (2010).
19. S. G. Adie et al., "Audio frequency in vivo optical coherence elastography," *Phys. Med. Biol.* **54**(10), 3129–3139 (2009).
20. B. F. Kennedy et al., "In vivo dynamic optical coherence elastography using a ring actuator," *Opt. Express* **17**(24), 21762–21772 (2009).
21. B. F. Kennedy et al., "In vivo three-dimensional optical coherence elastography," *Opt. Express* **19**(7), 6623–6634 (2011).
22. S. Wang et al., "Noncontact measurement of elasticity for the detection of soft-tissue tumors using phase-sensitive optical coherence tomography combined with a focused air-puff system," *Opt. Lett.* **37**(24), 5184–5186 (2012).
23. X. Liang et al., "Optical micro-scale mapping of dynamic biomechanical tissue properties," *Opt. Express* **16**(15), 11052–11065 (2008).
24. A. Srivastava et al., "Determination of elastic properties of resected human breast tissue samples using optical coherence tomographic elastography," *Strain* **47**(1), 75–87 (2011).
25. C. Li et al., "Quantitative elastography provided by surface acoustic waves measured by phase-sensitive optical coherence tomography," *Opt. Lett.* **37**(4), 722–724 (2012).
26. S. Li et al., "Toward soft-tissue elastography using digital holography to monitor surface acoustic waves," *J. Biomed. Opt.* **16**(11), 116005 (2011).
27. A. Curatolo et al., "Ultrasound-guided optical coherence tomography needle probe for the assessment of breast cancer tumor margins," *Am. J. Roentgenol.* **199**(4), W520–W522 (2012).
28. N. Iftimia et al., "Spectral-domain low coherence interferometry/optical coherence tomography system for fine needle breast biopsy guidance," *Rev. Sci. Instrum.* **80**(2), 024302–024302-9 (2009).
29. R. A. McLaughlin et al., "Imaging of breast cancer with optical coherence tomography needle probes: feasibility and initial results," *IEEE J. Sel. Top. Quantum Electron.* **18**(3), 1184–1191 (2012).
30. R. A. McLaughlin et al., "Static and dynamic imaging of alveoli using optical coherence tomography needle probes," *J. Appl. Physiol.* **113**(6), 967–974 (2012).
31. B. C. Quirk et al., "In situ imaging of lung alveoli with an optical coherence tomography needle probe," *J. Biomed. Opt.* **16**(3), 036009 (2011).
32. Y. Wu et al., "Robust high-resolution fine OCT needle for side-viewing interstitial tissue imaging," *IEEE J. Sel. Top. Quantum Electron.* **16**(4), 863–869 (2010).
33. K. M. Kennedy et al., "Needle optical coherence elastography for tissue boundary detection," *Opt. Lett.* **37**(12), 2310–2312 (2012).
34. A. E. Siegman, *Lasers*, University Science Books, Sausalito, California (1986).
35. R. K. Wang, Z. Ma, and S. J. Kirkpatrick, "Tissue Doppler optical coherence elastography for real time strain rate and strain mapping of soft tissue," *Appl. Phys. Lett.* **89**(14), 144103 (2006).
36. O. A. Shergold and N. A. Fleck, "Mechanisms of deep penetration of soft solids, with application to the injection and wounding of skin," *Proc. R. Soc. Lond. A Math.* **460**(2050), 3037–3058 (2004).
37. B. F. Kennedy et al., "Strain estimation in phase-sensitive optical coherence elastography," *Biomed. Opt. Express* **3**(8), 1865–1879 (2012).

38. K. M. Kennedy et al., "Measuring elastic contrast in tissue using OCT needle probes," *Proc. SPIE* **8571**, 857122 (2013).

39. K. M. Kennedy et al., "Analysis of mechanical contrast in optical coherence elastography," *J. Biomed. Opt.* **18**(12), 121508 (2013).

40. P. Schedin and P. J. Keely, "Mammary gland ECM remodeling, stiffness, and mechanosignaling in normal development and tumor progression," *Cold Spring Harb. Perspect. Biol.* **3**(1), a003228 (2011).

41. R. A. McLaughlin et al., "Parametric imaging of cancer with optical coherence tomography," *J. Biomed. Opt.* **15**(4), 046029 (2010).

42. D. Lorenser et al., "Dual-modality needle probe for combined fluorescence imaging and three-dimensional optical coherence tomography," *Opt. Lett.* **38**(3), 266–268 (2013).

43. G. Lamouche et al., "Review of tissue simulating phantoms with controllable optical, mechanical and structural properties for use in optical coherence tomography," *Biomed. Opt. Express* **3**(6), 1381–1398 (2012).

44. A. Latrive and A. C. Boccara, "In vivo and in situ cellular imaging full-field optical coherence tomography with a rigid endoscopic probe," *Biomed. Opt. Express* **2**(10), 2897–2904 (2011).

45. J. Wu et al., "Paired-angle-rotation scanning optical coherence tomography forward-imaging robe," *Opt. Lett.* **31**(9), 1265–1267 (2006).

46. D. Lorenser et al., "Ultrathin side-viewing needle probe for optical coherence tomography," *Opt. Lett.* **36**(19), 3894–3896 (2011).

47. L. Scolaro et al., "High-sensitivity anastigmatic imaging needle for optical coherence tomography," *Opt. Lett.* **37**(24), 5247–5249 (2012).

48. X. Liang et al., "Acoustomotive optical coherence elastography for measuring material mechanical properties," *Opt. Lett.* **34**(19), 2894–2896 (2009).

49. M. Razani et al., "Feasibility of optical coherence elastography measurements of shear wave propagation in homogeneous tissue equivalent phantoms," *Biomed. Opt. Express* **3**(5), 972–980 (2012)

50. B. Y. Yeo et al., "Enabling freehand lateral scanning of optical coherence tomography needle probes with a magnetic tracking system," *Biomed. Opt. Express* **3**(7), 1565–1578 (2012).

51. A. Ahmad et al., "Sonification of optical coherence tomography data and images," *Opt. Express* **18**(10), 9934–9944 (2010).

52. N. Sanai and M. S. Berger, "Glioma extent of resection and its impact on patient outcome," *Neurosurgery* **62**(4), 753–766 (2008).

53. S. D. Kundu et al., "Potency, continence and complications in 3,477 consecutive radical retropubic prostatectomies," *J. Urol.* **172**(6), 2227–2231 (2004).